ADVANCED SENSOR RESEARCH

Open Access

RESEARCH ARTICLE

ADVANCED
SENSOR
RESEARCH
Open Access

www.advsensorres.com

Nonlinear Damping as the Fourth Dimension in Optical Fiber Anemometry

*Jeremiah C. Williams and Hengky Chandrahalim**

In this study, nonlinear damping is introduced as the fourth dimension in the operation of a fiber tip optomechanical anemometer. The flow sensing element, featuring a 3D rotor measuring 110 µm in diameter and fabricated through a two-photon nanomachining process, is monolithically integrated onto the cleaved face of the optical fiber, which serves as an integrated waveguide. As the rotor encounters airflow, it spins, and mirrors on its blades reflect light across the fiber core at each pass. This setup permits precise measurement of gaseous fluid flow with minimal sensor footprint at the point of detection and accommodates a variety of optical sources and measurement apparatuses without the need for specific wavelength or broad-spectrum capabilities. To stabilize the rotation of the rotor and facilitate consistent frequency-domain analysis, a polydimethylsiloxane hydrocarbon stabilizing agent is infused into the gap between the rotor and stator of the sensing element via dual-function microfluidic channels. This enhancement allows for the measurement of gaseous nitrogen flow rates from 10 to 20 liters per minute (LPM), with a consistent periodic response. Comprehensive characterizations of the fiber tip anemometer are presented with and without the stabilizing medium, demonstrating its crucial role in regulating the dynamics between the rotor and the stator.

1. Introduction

Optical fiber-based sensors represent a dynamic field of research with diverse applications across aerospace systems, underwater drones, unmanned aerial vehicles (UAVs), biomedical monitoring, and environmental monitoring. These sensors benefit from various microfabrication techniques that facilitate the monolithic integration of sensing elements with an optical fiber, serving as a waveguide. Characterized by their lightweight, compact footprint, low power requirements, and high sensitivity, these sensors can detect a wide array of phenomena. Research in this area has led to the development of optical fiber sensors for an extensive range of applications. These include salinity sensing,[1] glucose detection,[2] temperature measurement,[3–7] refractive index assessment,[8,9] strain measurement,[10] deflection sensing between two surfaces,[11] detection of single nanoparticles,[12] magnetic field sensing,[13,14] acoustic detection,[15–17] advanced noise rejection in O_2 concentration sensing,[18] and flow measurement.[19–21] Similar sensors are also useful in biomedical applications, as exemplified by an ultrasensitive method for detecting virus microparticles described in the literature. This method utilizes polyvinylidene fluoride (PVDF) nanofibers with magnetostatic micromechanical actuation to achieve high sensitivity.[22]

Gaseous fluid flow sensing, the focus of this study, is a domain where microscale fiber optic sensors can significantly enhance capabilities. Relatively small and efficient sensors have been in use for flow sensing and anemometry for several decades,[23] but fiber-optic waveguides and emerging microfabrication techniques present a path for significant miniaturization of these technologies. The lightweight nature of these sensors provides substantial benefits for mass-sensitive systems, such as microsatellites, in vivo biosensors, underwater drones, spacecraft, and UAVs. Moreover, their compact footprint facilitates detailed flow field mapping and allows for the integration of numerous sensor arrays within targeted applications. A light-based signal, when used in conjunction with emerging materials, also tends to outperform electrical sensing elements in environments with high heat and radiation.

Previously, researchers have developed an anemometer that includes a silicon film attached to an optical fiber, which is heated by a coaxial laser.[24] The resonant wavelength of this Fabry–Pérot (FP) cavity changes as the incident gas flow cools the silicon, altering its refractive index and length. Although this design is robust, it requires a sufficiently powerful laser to heat the silicon film effectively. Water flow sensing has been accomplished by tracking the deflection of a gold reflector positioned opposite an optical fiber, though this component is significantly larger than the fiber itself.[25] Another approach has used a fiber FP cavity to detect the

J. C. Williams, H. Chandrahalim
Department of Electrical and Computer Engineering
Air Force Institute of Technology
Wright-Patterson Air Force Base, Dayton, OH 45433, USA
E-mail: hengky@microsystems.group

The ORCID identification number(s) for the author(s) of this article can be found under https://doi.org/10.1002/adsr.202400080

**ADVANCED
SCIENCE NEWS**

www.advancedsciencenews.com

**ADVANCED
SENSOR
RESEARCH**
Open Access

www.advsensorres.com

deflection of a gold membrane in response to dynamic pressure from incoming flow, successfully measuring wind speeds up to 300 m s^{-1} in a wind tunnel.[26] Human breath has similarly been measured through the deflection of a micro cantilever caused by exhaling, forming an FP cavity at the tip of an optical fiber.[27] These FP cavity sensors are highly sensitive but depend on either broad-spectrum analysis to monitor the Vernier effect or a single wavelength to track resonance shifts, which both require specialized equipment for production and analysis.

Another sensitive optical fiber-based gaseous flow sensor measures the displacement of a fiber running through the flow path, projecting light onto a photocurrent detector mounted on the opposite side of the flow path.[28] This method offers high sensitivity but is limited to flow regimes that do not displace the projecting fiber off the sensor, and it must be fixed at two locations, extending through the flow path. A similar deflection-based fiber sensor utilizes the bending of an integrated fiber Bragg grating cladding and the corresponding shift in peak intensity of the cladding's resonance to measure low flow rates.[29] However, this device also introduces a non-negligible target into the flow path and requires gravity-dependent mounting from the top of the flow path. Another device measures the shift in resonant wavelength between two Bragg gratings coupled to an optical fiber that is inserted on a thin, cylindrical cantilever into incident flow.[30] This device is simple to fabricate and robust in operation but, as presented, requires both a broad-spectrum light source and precise spectral analysis equipment.

The fiber tip optomechanical flow sensor showcased in this work employs a micro-rotor to maintain a diminutive sensing element that can operate with low-power light across a flexible bandwidth. This design enables the sensor system to function with smaller, simpler devices for light generation and analysis. It also facilitates the direct, real-time transmission of detected flow rates via low-loss optical fiber to remote locations, eliminating the need for additional packaging to support signal routing.

Researchers have explored the application of nonlinear damping within the context of fractal oscillators. Their study offers a compelling perspective on how nonlinear dynamics can be incorporated into fractal spaces to influence system behavior. While their approach involves the use of fractal spaces to incorporate nonlinear dynamics, our work introduces nonlinear damping as an additional dimension in the traditional x, y, and z spatial framework. This dimension is introduced alongside the x, y, and z spatial dimensions and plays a pivotal role in stabilizing the sensor's dynamic response. The nonlinear damping, facilitated by a polydimethylsiloxane hydrocarbon stabilizing agent, interacts with the physical dimensions to enhance the anemometer's performance and sensitivity. Moreover, it effectively mitigates dry adhesive friction and rotational instability, which are factors that can complicate flow sensing. By highlighting this distinction, we aim to clarify our conceptual framework and its unique contributions to the field of optomechanical sensing.[31] **Figure 1** showcases the optomechanical flow sensor fabricated on the flat end of an optical fiber.

As illustrated in Figure 1, the sensing element, despite its small size, features a complex 3D aerodynamic geometry. This level of complexity, coupled with the use of a non-traditional fiber optic platform as the host, surpasses the capabilities of standard photolithography for patterning this type of sensor element.
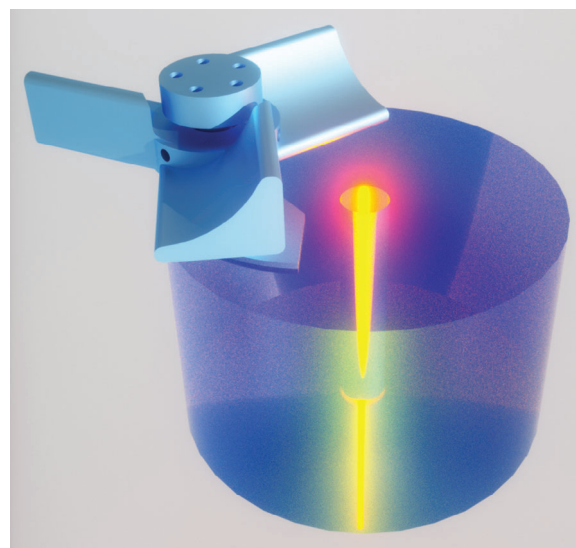

Figure 1. Schematic illustration of the 3D optomechanical flow sensor, fabricated on the flat end of an optical fiber. The sensing element includes a rotor, which measures 110 μm in diameter and revolves around a stator.

To fabricate our device, we utilized the two-photon polymerization (2PP) microfabrication technique. This maskless nanomachining technique has been employed to create a variety of devices on the tips of optical fibers. Examples include the previously mentioned breath sensor,[27] a glucose detector formed by a suspended Fabry–Pérot cavity,[2] a spiral spring acoustic wave sensor,[32] and a combined parabolic lens with a helical axicon for beam shaping.[33] Moreover, the 2PP nanomachining method has been successfully used to integrate micromechanical components with optical cavities,[34–36] enabling advanced sensors on optical fiber tips, such as those for pressure,[19,37] temperature,[3] and refractive index measurements.[8]

The optomechanical flow sensor we present here features a 3D rotor with a diameter of 110 μm, which revolves around a stator fabricated using a 2PP nanomachining process. The anemometer is fabricated directly onto the cleaved face of an optical fiber which then serves as a monolithically integrated optical waveguide. As the rotor encounters incident fluid flow, the rotor spins in response causing mirrors on its blades to pass over the fiber core and reflect light back through the fiber. This sensing mechanism enables precise measurement of fluid flow with a minimal sensor footprint at the point of detection. The design also accommodates various optical sources and measurement devices, and does not require bulky equipment to monitor a specific wavelength or a broad-spectrum response. A polydimethylsiloxane hydrocarbon stabilizing or damping agent is injected into the space between the rotor and stator via dual-function microfluidic channels. This serves to stabilize the rotor's movement and produce a consistent response for frequency-domain analysis. The integration of this stabilizing medium produces a consistent, periodic response to gaseous nitrogen flow rates ranging from 10 to 20 LPM and enables frequency-domain analysis across this range. The fiber tip anemometer is characterized both with and without the damping medium to demonstrate the critical role of the damping medium in regulating the dynamics between the

2400080 (2 of 15)

ADVANCED
SCIENCE NEWS

www.advancedsciencenews.com

ADVANCED
SENSOR
RESEARCH
Open Access

www.advsensorres.com

rotor and stator to enable reliable and periodic sensing. Additionally, systematic analysis of potential factors influencing the anemometer's nonlinear response is elucidated. The advantages of nonlinear systems in sensing, based on the results produced by our device, are highlighted. This study lays the groundwork for further exploration of highly integrated sensing elements comprising complex, compact, and dynamic 3D mechanical and optical components, which are difficult to produce with current industrial fabrication technology. This research also paves the way for nonlinear optomechanical sensing applications in space-constrained environments.

2. Results and Discussion

2.1. Design and Principle of Operation

The anemometer design developed in this work draws inspiration from the mechanics of a traditional wind turbine, where air flow impinging on the turbine blades introduce drag forces which cause rotation. This principle guided the design of our flow sensor's rotor, incorporating cup-like blades as depicted in **Figure** 2a to harness rotation from the incident flow. To optimize the design, it was essential to establish a clear on-off condition for light reflection. Lift-driven blade designs using thin, angled blades were initially considered; however, these blades tended to scatter the incident light, and failed to provide a distinct reflection as they passed over the fiber core. To improve the reflection signal quality, the blades were designed with flat bottoms, improving the time and angle of light reflection back down the fiber core. Additionally, a curved top was introduced to the three microblades to increase the surface area interacting with the flow and direct the driving rotational forces, thereby enhancing the sensor's responsiveness.

The 55 μm rotor blade length was selected to produce a slope to the support material that could be successfully fabricated reliably, ≈60° at the steepest, and to prevent sagging during polymerization. Unsupported blades experienced significant warping upon release, where the chosen geometry and support system remained largely perpendicular to the fiber face. Various factors, including the aerodynamic features in the blade's profile and the overall size and number of blades, can be explored in a targeted design experiment to further refine the device going forward. The geometry presented also exhibited the most stable spin out of several blade iterations attempted during development.

The dynamic assembly, as illustrated in Figure 2a, features a rotor that rotates around a stator affixed to the cleaved face of an optical fiber, reacting to axial fluid flow impacting three cup-like microblades. The rotor spins faster under higher flow rates. Each blade's bottom is a flat optical surface coated with highly reflective gold, aligned parallel to the fiber face. As the rotor spins, these mirrors sequentially pass over the fiber core, reflecting light back through the fiber whenever they align with the core. The rotor responds primarily to flow from the axial direction, perpendicular to the face of the fiber. Although the device cannot currently indicate the direction of the flow on its own, multiple devices at different orientations could be fused together to determine the flow direction in future applications of the anemometer.

Given the conditions under which this device operates, the flow regime was determined to be incompressible, with a Mach number calculated at 0.15 for the highest observed flow rate. This value is well below the threshold of 0.3 that typically indicates a transition to compressibility.[38] The dynamic pressure from the flow is calculated using the formula $P = \rho v^2/2$, where ρ is the density of the flow and v is the velocity of the flow. The microblade design induces both radial and axial reaction forces; the radial force facilitates rotation, while the axial force presses the rotor against the stator base. Rotation is resisted by the drag of the blades, along with friction at both the center post and the base of the stator.

The fiber acts as a low-loss waveguide, allowing the light source and measurement equipment to be distanced from the sensing point. At the fiber's opposite end, the reflected light is isolated by an optical circulator and measured using an optical power meter and oscilloscope. The frequency of these reflection events correlates with the rotor's rotational velocity, which depends on the velocity of the incident flow.

The dynamics involved in flow sensing experiments are often more complex than those described by theoretical analytic models. In order to gain a more realistic perspective on the operation of this fiber optic flow sensor, a computational fluid dynamics (CFD) analysis was performed using Ansys Fluent. Additional information related to the parameters used in the CFD analysis conducted in this study is available in the Experimental section (Section 4). The 3D image in Figure 2b qualitatively illustrates several random path lines surrounding the blades and the fiber tip and highlights areas of high pressure located behind, underneath, and in front of the microblade. These areas indicate significant out-of-plane flow (directed toward the post) caused by the fiber face. Upon examining the top and bottom of the rotor, one can observe the varying pressures that the individual blades experience as they pass over the fiber. This complex aerodynamic situation can lead to irregular rotation of the microblades. Additionally, as depicted in Figure 2a, there is a 2 μm air gap between the rotor and stator. This gap facilitates dry adhesive friction and rotation instability between the rotor and stator, which may cause issues with the stability of the response during flow sensing experiments.

In order to address the stability issues, five 4-μm diameter dual-function microfluidic channels were designed, one of which is shown in the cross-sectional image in Figure 2a. This channel serves a dual purpose: delivering developer fluid to cure the photosensitive resin and aiding the transport of stabilizing agent into the gap between the stator and rotor. This microfluidic design ensures precise fluid management, optimizing both the resin development process and the stabilization of mechanical components within the fiber tip anemometer microsystem.

2.2. Fabrication Process

The device was fabricated using the 2PP nanomachining technique with the Nanoscribe GT Photonic Professional 2PP system. This method solidifies photoactive resin similarly to stereolithography but utilizes two photons at half the wavelength required for single-photon polymerization to impart the resin's polymerization energy. The precision of the laser beam allows for the creation of voxels (3D pixels) as small as 200 nm × 200 nm × 200 nm. This resolution is significantly higher than standard

ADVANCED
SCIENCE NEWS

www.advancedsciencenews.com

ADVANCED
SENSOR
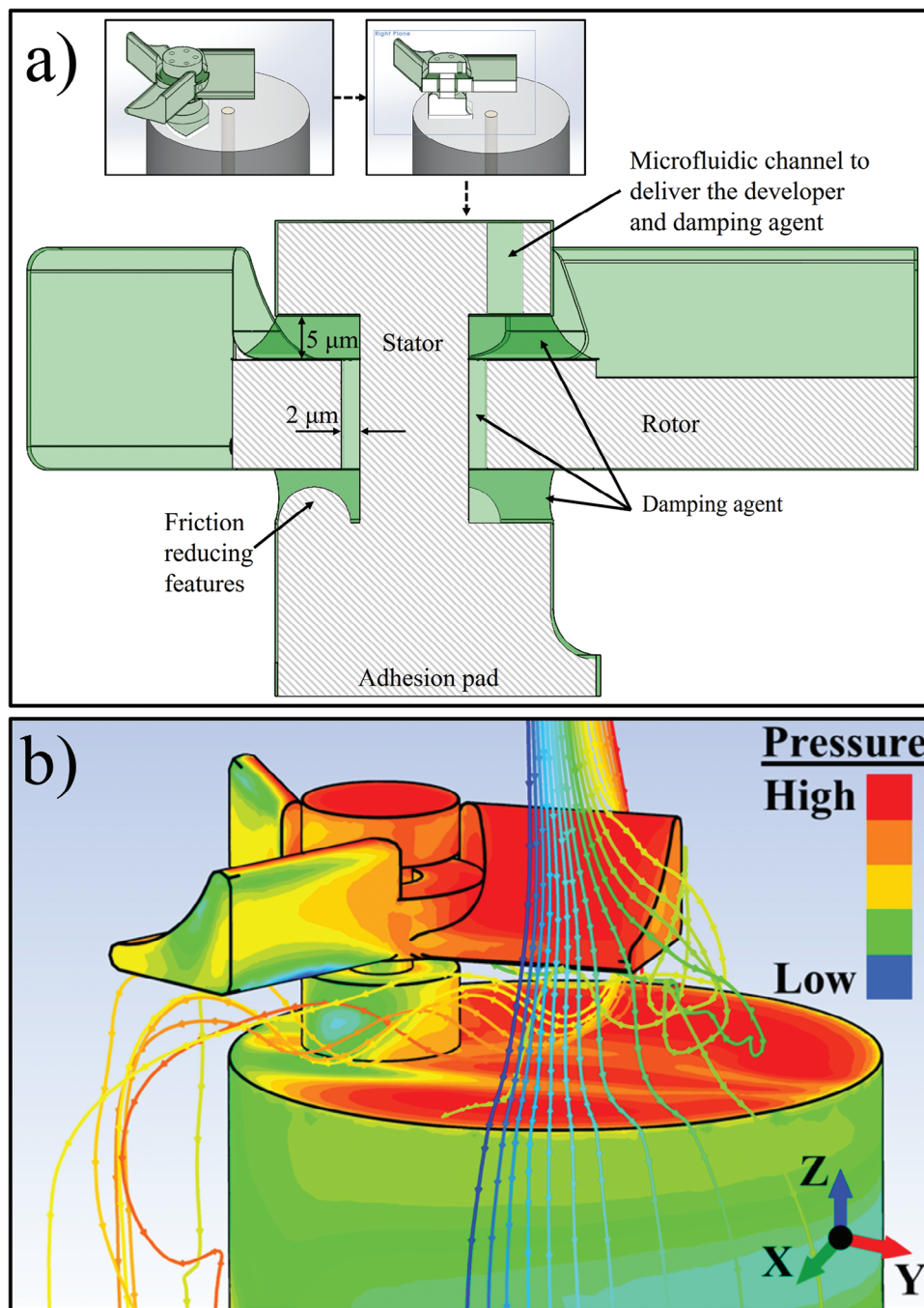**RESEARCH**
Open Access

www.advsensorres.com

Figure 2. a) Schematic depicting the design details of the fiber tip anemometer, including the rotor, stator, and microblades. The cross-sectional diagram highlights one of the five 4-µm diameter microfluidic channels, which are used for delivering both the resin developer fluid and the damping agent. These channels facilitate precise fluid management, optimizing both the development process and the stabilization of mechanical components within the system. b) Computational fluid dynamics analysis examining the complex aerodynamic effects on the microblades and the fiber tip. The simulated 3D image displays erratic path lines around the microblades and the fiber tip. Different colors represent varying pressures, while the flow lines are distinctly colored to enhance visual clarity.

3D printers,[39] and approaches the resolution available in immersion lithography technology.[40] As with 3D printing, the laser is directed through the resin according to a 3D computer-aided design (CAD) model. The model is processed by Nanoscribe software to "slice" the geometry into discrete layers of a cho-

sen height. Each 2D layer is polymerized individually before the fiber substrate is raised for the next layer to additively manufacture the desired structure. The detailed laser inscription process for the fiber tip optomechanical anemometer is depicted in **Figure 3**a–e.

ADVANCED
SCIENCE NEWS

www.advancedsciencenews.com

ADVANCED
SENSOR
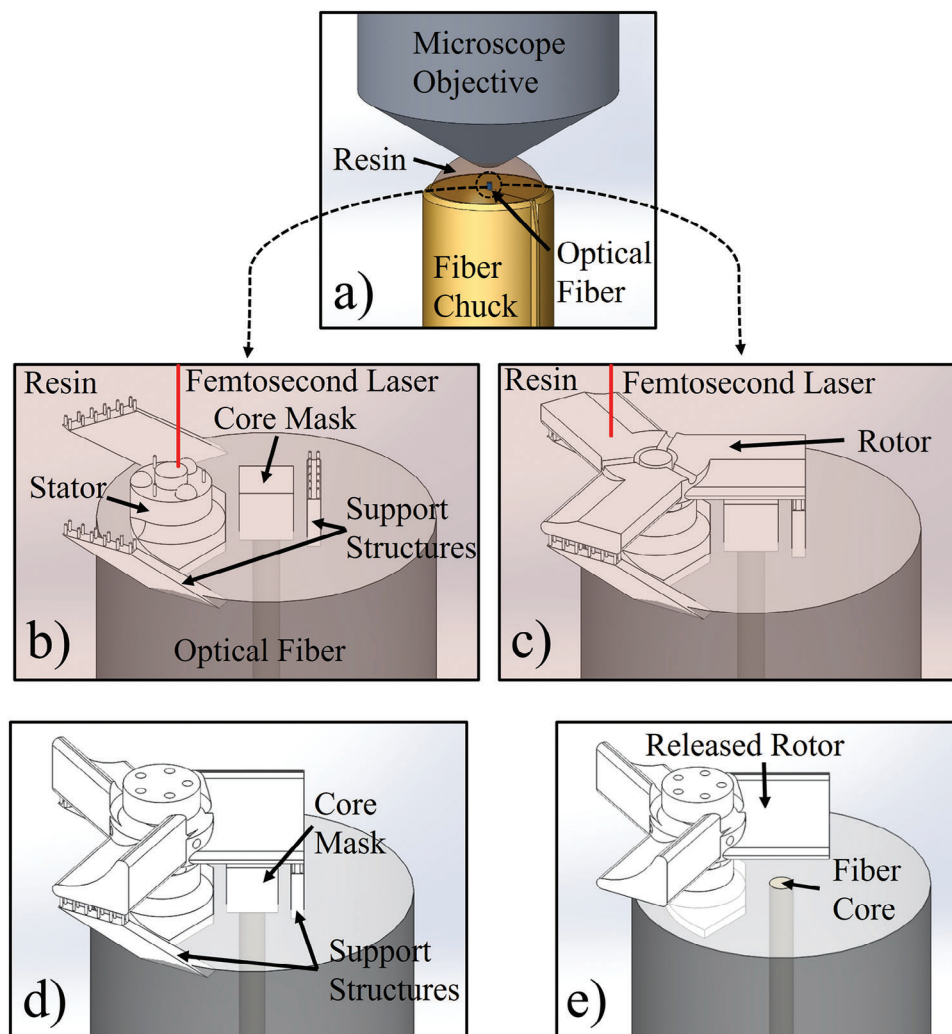**RESEARCH**
Open Access

www.advsensorres.com

Figure 3. Graphical depiction of the 2PP fabrication process used to create a fiber tip optomechanical flow sensor. a) Macro view schematic illustrating the microscope objective used to focus femtosecond laser pulses for polymerizing the resin, which was immersed in a drop of resin on top of the fiber chuck surrounding the fiber tip. b,c) Cross-sectional views depicting various stages of polymerization. d) The device after cleaning with isopropyl alcohol (IPA), shown polymerized with the masking brick and support structures still in place. e) Schematic of the fiber tip anemometer after deposition of the reflective coating, with supports and masking brick removed.

During fabrication, a cleaved fiber was secured in a side-loading fiber chuck, and a drop of photoactive resin was deposited onto the chuck's face to envelop the fiber. The fiber was aligned with the laser using a custom jig attached to the Nanoscribe's sample mounting plate, as shown in Figure 3a. The anemometer features a lateral resolution of 200 nm × 200 nm and layer heights of 300 nm. The design includes breakable support structures for each rotor blade and a masking cap over the fiber core. Twelve 1 µm pillars connect the blades to the support structures, and a 20 µm cube serves as the masking cap. The stator's inner pillar has a diameter of 12 µm with a clearance of 2 µm from the rotor.

Five 4-µm diameter dual-function microfluidic channels were incorporated to facilitate the entry of both propylene glycol monomethyl ether acetate (PGMEA) solution to develop the photosensitive resin within the tight clearances and the damping agent between the stator and rotor to improve rotational stability. Additionally, three hemispherical features were patterned on

the base of the stator to minimize friction with the rotor. The non-polymerized resin was developed in PGMEA for 20 min. Halfway through this process, the fiber was extended several millimeters for the final 10 min to prevent resin droplets from forming around the device. Subsequently, the device was cleaned in isopropyl alcohol (IPA) for 10 min to remove any residual PGMEA, as illustrated in Figure 3d.

The support structures that maintained the microblades during the 2PP process, shown in Figure 3b–d, were carefully removed with a semiconductor analysis probe. This procedure required similar manual dexterity as needed for precise wire bonding or device probing. Additional details about the 2PP process parameters and the photosensitive resin used in fabricating the fiber tip flow sensors are available in the Experimental Section (Section 4).

A reflective gold film was deposited onto the device using a magnetron sputtering system. The device was positioned on a
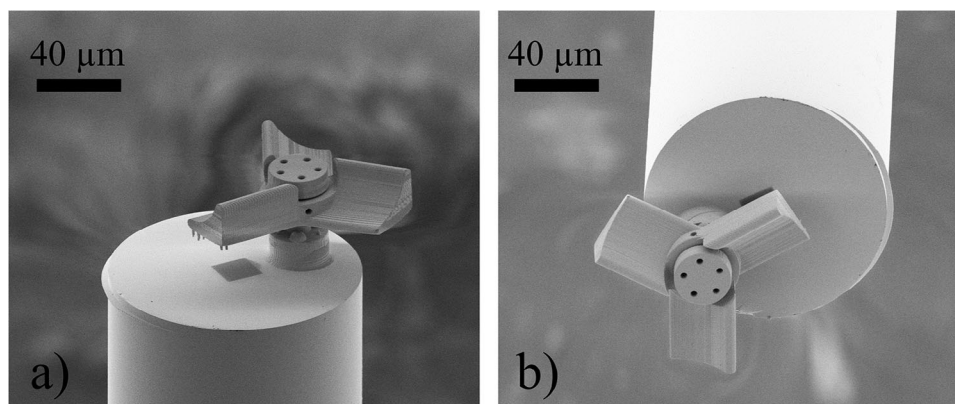
ADVANCED
SCIENCE NEWS

www.advancedsciencenews.com

ADVANCED
SENSOR
RESEARCH
Open Access

www.advsensorres.com

Figure 4. Scanning electron microscope (SEM) images of the fiber tip anemometer after the removal of all support structures and the masking cap, showing a side view in image a) and a top view in image b).

rotating platen with the blades aligned approximately orthogonal to the sputtering target. The sputtering was conducted at a pressure of 5 mTorr and a power setting of 100 Watts for 5 min. While the gold film rendered the device visually reflective, determining the precise thickness of the coating proved challenging due to the angle of the blades relative to the target and interference from the fiber face.

During sputtering, a sacrificial polymer brick was placed over the fiber core to protect it. This brick was subsequently removed with a similar technique to removing the blade supports, performed most effectively by applying upward pressure with the very tip of the probe to peel it from the fiber tip. Following this procedure, the fiber tip anemometer was ready for testing. The final schematic of the anemometer after removing the support structures and sacrificial brick is depicted in Figure 3e. Additionally, scanning electron microscope (SEM) images of the fully fabricated and test-ready fiber tip anemometer are presented in **Figure** 4a,b. Further details regarding the gold sputtering process can be found in the Experimental Section (Section 4).

As previously discussed in Section 2.1, the complex aerodynamic environment around the sensing element at the fiber tip can cause sporadic and irregular rotation of the microblades in response to incident flow. Additionally, as illustrated in Figure 2a, a 2 μm air gap between the rotor and stator introduces dry adhesive friction and rotation instability, potentially complicating flow sensing experiments. To address these challenges, we explored the use of fluid quadrivium stabilizing agents, regarded as the fourth dimension of our sensor design. These agents can be introduced through five 4-μm diameter dual-purpose microfluidic channels into the anemometer to fill the 2 μm gap and stabilize the rotor's rotation.

We required a low-viscosity liquid capable of entering the tight clearances between sensing components with sufficiently low volatility to persist within the device long enough to support repeat sensing operations. We identified a suitable stabilizing agent, composed of 85–95% low volatile petroleum (LVP) aliphatic hydrocarbon and 1–5% polydimethylsiloxane, as an effective stabilizing agent. The high percentage of LVP aliphatic hydrocarbon ensures low volatility, enhancing the oil's stability and consistency in performance, while the polydimethylsiloxane contributes to thermal stability and lubrication. This carefully bal-

anced formulation is ideal for use between the rotor and stator of the anemometer, where precise interaction with the device's components is crucial.

The application process, depicted in **Figure** 5a, involved dripping the polydimethylsiloxane hydrocarbon damping medium over the entire structure. This was followed by ≈5 min of exposure to a heat gun to dry the device's exterior, as shown in Figure 5b, intended to remove excess stabilizing medium from the surface of the device, but maintain stabilizing medium within the clearances between the rotor and stator. Figure 5c displays the fiber tip anemometer with the integrated polydimethylsiloxane hydrocarbon stabilizing medium, which is expected to stabilize the rotor's spin, allowing for reliable measurement and extraction of rotational frequency.

2.3. Characterization

2.3.1. Measurement Setup

The measurement setup for the fiber tip optomechanical anemometer is illustrated in **Figure** 6. The device under test (DUT) was secured within a 1/4-inch diameter side-loading fiber chuck and attached to a mirror mount using the appropriate adapter. Nitrogen flow, the subject of measurement, was directed through a flow meter and emitted from a 1/8-inch pressure fitting used as the nozzle. The DUT was precisely aligned to the nozzle using the mirror mount while monitoring under a microscope to achieve the fastest rotor rotation at an arbitrary initial flow rate.

For illumination down the optical fiber, a superluminescent diode was connected to the first port of an optical circulator, serving as the light source. Importantly, the wavelength of the light for this sensor is not critical to our measurement scheme; therefore, any wavelength that can propagate through the fiber is suitable. The DUT was connected to the second port of the optical circulator, with the reflective output isolated and collected at the third port. This light output was measured using an optical power meter and recorded by a digital oscilloscope. Alternative sensing equipment, such as a diode light source and a photodiode detector, could be used in place of the optical power meter
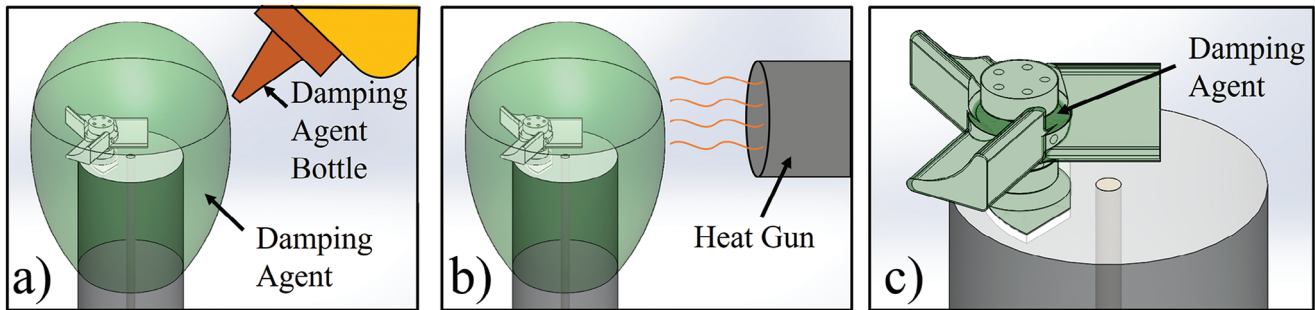
Figure 5. Schematic illustrating: a) application of the polydimethylsiloxane hydrocarbon stabilizing agent, dripped over the entire surface of the fully released flow sensor head; b) drying of the stabilizing agent with a heat gun, with excess being removed; and c) the fiber tip anemometer with the integrated damping agent.

and oscilloscope to achieve a more compact system design. Additional information about the equipment and components used in the characterization of the optomechanical flow sensors in this study is available in the Experimental section (Section 4).

The nitrogen flow was incrementally increased, with each level maintained for at least 60 s to ensure the rotor's rotation was stable before recording the data. Both the reference flowmeter and the device rotor responded and stabilized within 1–3 s of initiating flow. The 60-s hold time was chosen to eliminate any potential inconsistencies due to starting friction, ensuring that the measured response was not influenced by transient effects. This procedure was repeated twice, with the flow returned to zero between trials, and the orientation of the device was maintained consistently throughout the measurements.

Occasionally, the fiber tip anemometer generated reflection peaks with varying amplitudes. This was caused by changes in the angle between the rotor mirrors and the fiber face. This variability complicated frequency domain analysis, as lower frequencies tended to artificially dominate the analysis. To mitigate this issue, the raw data from the oscilloscope underwent several processing steps: first, taking the absolute value to eliminate noise below zero; then, normalizing each measurement on a scale from one to one hundred based on the minimum and maximum intensity values. Subsequently, the logarithm of the data was subjected to a fast Fourier transform (FFT). This processing strategy reduced the impact of amplitude variation and allowed the FFT to consistently identify the dominant frequency that was observed in qualitative assessments.

The algorithm employed to process the oscilloscope data is both straightforward and practical, ensuring ease of implementation for real-world applications of the fiber tip optomechanical anemometer. By utilizing a series of concise steps — taking
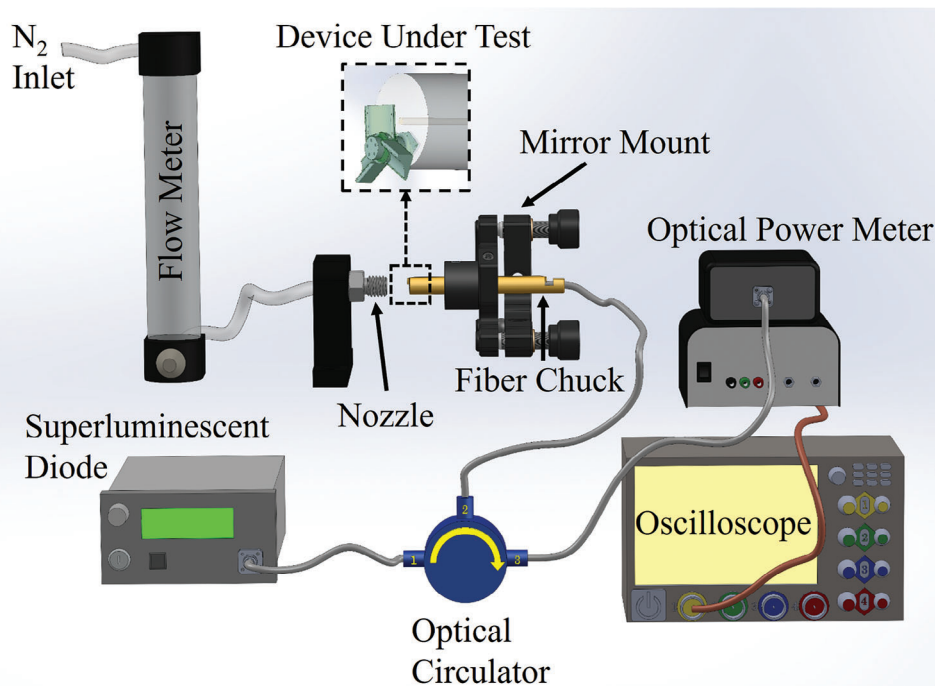

Figure 6. Schematic illustrating the measurement setup used to characterize the fiber tip optomechanical anemometer.

ADVANCED
SCIENCE NEWS

www.advancedsciencenews.com

ADVANCED
SENSOR
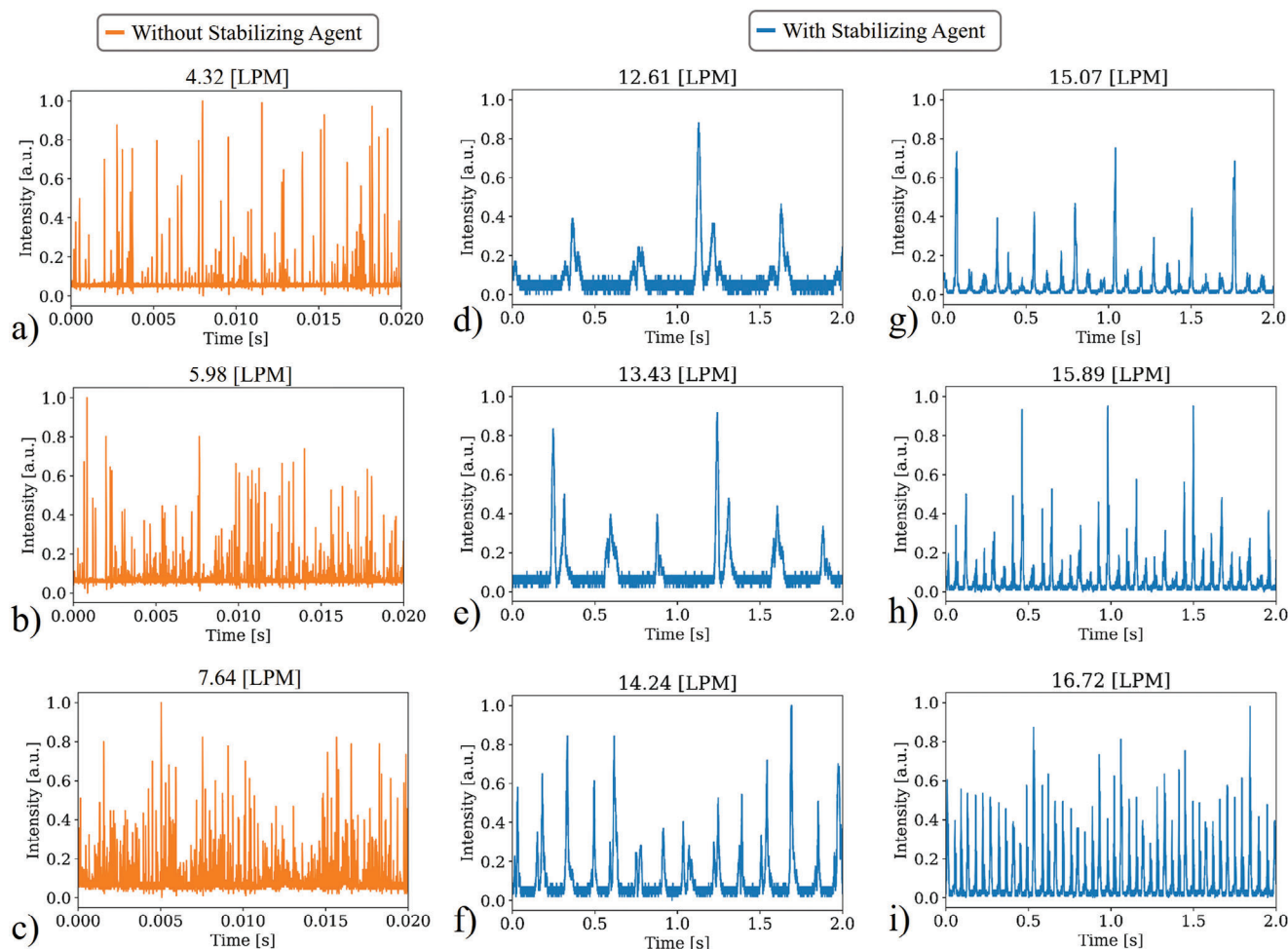**RESEARCH**
Open Access

www.advsensorres.com

Figure 7. Sample reflection spectra from the fiber tip optomechanical anemometer at various flow rates. Panels a–c) display typical results from the device without the stabilizing medium, where the erratic and irregular nature of the reflection spectra is evident on a short, 0.02-s time scale. This suggests that the device began to spin at a lower flow rate but failed to maintain a consistent frequency. Panels d–i) present sample reflection spectra from the flow sensor after the injection of the stabilizing medium between the rotor and stator of the anemometer. A consistent frequency of reflection events is observed over the entire 2-s time scale.

absolute values, normalizing measurements, taking the logarithm, and applying an FFT — this method effectively minimizes amplitude variation and reliably identifies dominant frequencies. Such simplicity in data processing not only enhances the usability of the anemometer in diverse settings but also ensures that users can achieve accurate and consistent results without the need for complex computational resources.

2.3.2. Measurement Results

The device was measured both before and after the injection of the stabilizing medium. The flow sensor's responses without a damping medium at three flow rates are presented in **Figure** 7a–c. Responses with a damping agent at six different flow rates are reported in Figure 7d–i. Without the stabilizing medium, the device began to spin at a lower flow rate but did not maintain a consistent frequency. In contrast, the flow sensor with a damping medium demonstrated a clearly periodic response, fa-

cilitating precise frequency domain analysis. The anemometer's responses were analyzed using an FFT, as previously described in Section 2.1.1, and dominant frequency components were clearly evident.

The frequency domain response of each measurement from the flow sensor with an integrated damping agent is presented in **Figure** 8a. The spectral blur observed at higher flow rates was attributed to the physical shaking of the fiber, as visually observed through the optical microscope at these higher flow rates. In operational flow sensing measurements, a robust ferrule that encases the exposed fiber section will be necessary to eliminate this undesired physical vibration and to allow for a broader measurement range. The average of the four most prominent frequency components was taken as the sensed result of the flow. The extracted frequencies as a function of flow rate are plotted in Figure 8b, with the mean and standard deviation calculated from the two recorded experiments. The response fits well to a second-order polynomial and offers significantly improved consistency compared to the anemometer without a stabilizing agent. The
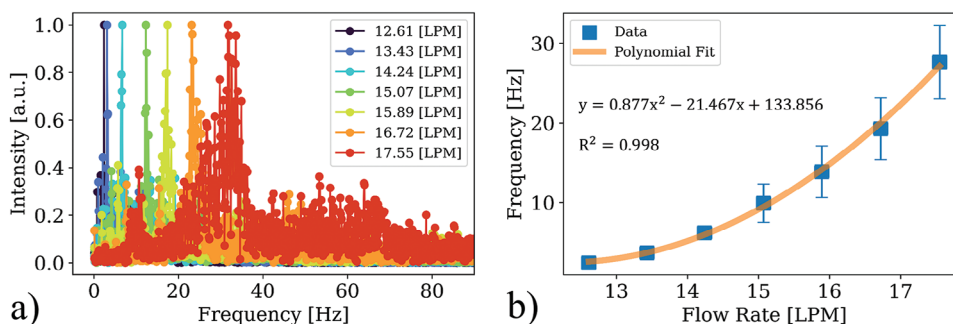
ADVANCED
SCIENCE NEWS

www.advancedsciencenews.com

ADVANCED
SENSOR
RESEARCH
Open Access

www.advsensorres.com

Figure 8. Frequency response of the fiber tip optomechanical anemometer with an integrated stabilizing agent. Panel a) presents the Fourier transform of the reflection spectra, highlighting a clear dominant frequency that increases as a function of flow rate. Panel b) plots the mean of the four highest intensity frequencies from the Fourier transform at each flow rate, including two sets of measurements. The error bars represent one standard deviation, and the boxes indicate the mean of these two measurements. One-way analysis of variables (ANOVA) between the flow rates and the measured frequency indicates an F-statistic of 10.91 and a P-value of 0.003. The orange line represents a polynomial-fit to the mean measurements, with a proportion of determination (R^2) value indicating a high proportion of the variation can be predicted with the calculated polynomial.

relationship between the rotor's rotational velocity and the velocity of the incident flow, along with the origin of the nonlinear response of the frequency as a function of flow rate depicted in Figure 8b, is explored in Section 2.4.

2.4. Analysis and Discussion

The shape of the microblades generates both radial and axial reaction forces. The radial force propels the rotation, while the axial force presses the rotor against the base of the stator. Opposition to the rotation arises from the drag of the blades, as well as friction at the center post and the base of the stator, as illustrated in **Figure 9**. In an idealized steady state, the forces acting on the rotor include the radial force due to the incident flow (F_{Inc_x}), the

drag force of the rotor blades (F_{Drag}), the friction force at the base of the stator (F_{Base}), and the friction at the stator post (F_{Post}). At a given steady state, these forces balance to zero net force, thereby maintaining a constant rotational velocity.

The rotational velocity of the rotor is directly related to the velocity of the incident flow, as demonstrated by taking the sum of moments around the central axis of the rotor. At steady state, this yields the following equation:

$$\sum M = M_{Inc\_x} - M_{Base} - M_{Post} - M_{Drag} = 0 \tag{1}$$

where M_{Inc_x}, M_{Base}, M_{Post}, and M_{Drag} are the moments generated by F_{Inc_x}, F_{Base}, F_{Post}, and F_{Drag}, respectively.
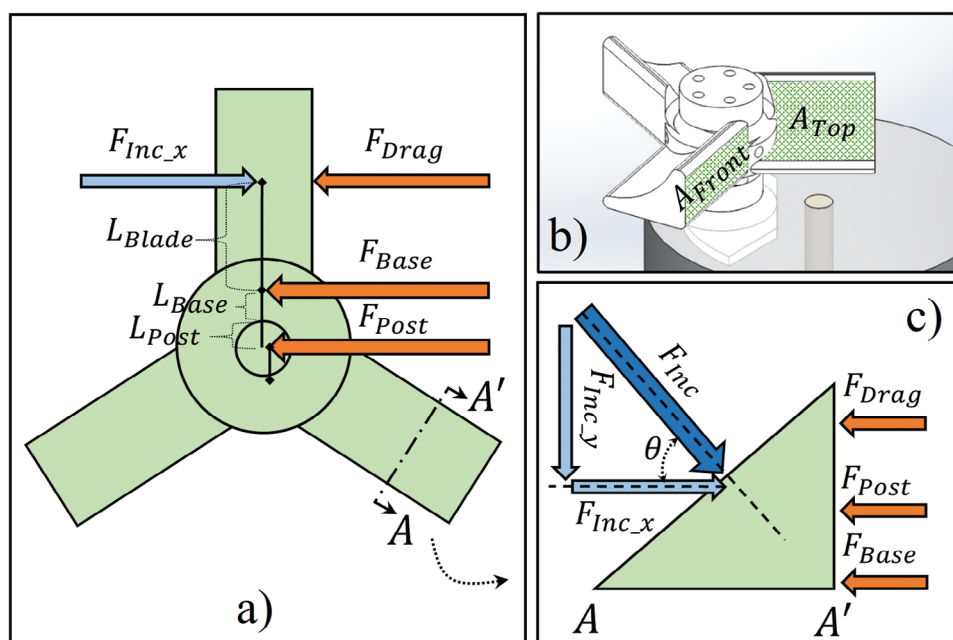

Figure 9. Schematic illustrating the forces acting on the fiber tip anemometer under incident airflow. In an idealized steady state, the forces on the rotor include the radial force due to the incident flow (F_{Inc_x}), the drag force of the rotor blades (F_{Drag}), the friction force at the base of the stator (F_{Base}), and the friction at the stator post (F_{Post}).

**ADVANCED
SCIENCE NEWS**

www.advancedsciencenews.com

**ADVANCED
SENSOR
RESEARCH**

www.advsensorres.com

Expanding Equation (1) to include the contributing forces results in the following expression:

$$F_{Inc\_x} \cdot L_{Blade} = \left[\mu_k \cdot F_{Inc\_y} \cdot L_{Base} \right] + \left[\mu_k \cdot \left(F_{Cent} + F_G \right) \cdot L_{Post} \right] + \left[F_{Drag} \cdot L_{Blade} \right] \tag{2}$$

where μ_k is the coefficient of kinetic friction, F_{Cent} is the centripetal force on the rotor, and F_G is the force of gravity acting on the rotor, given that the fiber is oriented horizontally during flow sensing. L_{Blade}, L_{Base}, and L_{Post} are the geometrical parameters defined in Figure 9. The anemometer studied here features three identical rotor blades. This configuration allows for the analysis of just one blade to understand the kinematics of the entire system. By expanding the forces described in Equation (2) for one rotor blade, we obtain the following expression:

$$\frac{1}{2} \rho_{N_2} v_{N_2}^2 A_{Top} \cos \theta \, L_{Blade} = \left[\mu_k \frac{1}{2} \rho_{N_2} v_{N_2}^2 A_{Top} \sin \theta L_{Base} \right] + \left[\mu_k \left(\frac{1}{3} m L_{Post} \omega^2 + \frac{1}{3} m g \right) L_{Post} \right] + \left[C_d A_{Front} \frac{\rho_{N_2} \left(L_{Blade} \omega \right)^2}{2} L_{Blade} \right] \tag{3}$$

where θ, A_{Top}, and A_{Front} are geometrical parameters defined in Figure 9. The variables ρ_{N_2}, v_{N_2}, m, C_d, g, and ω represent the density of the nitrogen flow, the velocity of the nitrogen flow, the mass of the rotor, the drag coefficient, the acceleration due to gravity, and the rotor's rotational velocity, respectively.

Equation (3) can be rearranged to reveal the relationship between the rotor's rotational velocity, ω, and the velocity of the incident flow, v_{N_2}, as shown in the following equation:

$$\omega^2 = v_{N_2}^2 \left[\frac{\left(\frac{1}{2} \rho_{N_2} A_{Top} \cos \theta L_{Blade} - \mu_k \frac{1}{2} \rho_{N_2} A_{Top} \sin \theta L_{Base} \right)}{\left(C_d A_{Front} \frac{1}{2} \rho_{N_2} L_{Blade}^3 + \mu_k \frac{1}{3} m L_{Post}^2 \right)} \right] - \left[\frac{\left(\mu_k \frac{1}{3} m g L_{Post} \right)}{\left(C_d A_{Front} \frac{1}{2} \rho_{N_2} L_{Blade}^3 + \mu_k \frac{1}{3} m L_{Post}^2 \right)} \right] \tag{4}$$

Equation (4) illustrates a linear relationship between the rotor's rotational velocity and the nitrogen flow velocity, which does not fully align with our experimental results. As shown in Figure 8, the experimental data demonstrate that the rotor's rotational velocity increases nonlinearly with the flow rate.

Aerodynamic effects, such as blade design and the angle of the rotor blades, can result in complex interactions with airflow, such as turbulence, which might not be linearly proportional to the flow rate. The efficiency with which each blade converts airflow into rotational motion can vary at different flow rates, potentially leading to nonlinear behavior. However, our design mitigates such effects. As depicted in Figure 9, the three drag-driven blades of our anemometer are engineered to prevent airflow separation from the blade surfaces, which can lead to a sudden loss of lift and an increase in drag in lift-driven blade designs. Our ex-

perimental results, presented in Figure 8, demonstrate that the rotational velocity of the rotor increases nonlinearly as a function of the flow rate, adhering to the second-order polynomial equation $y = 0.877x^2 - 21.467x + 133.856$, with $R^2 = 0.998$, where y is directly related to the rotational velocity, and x denotes the flow rate. This relationship strongly suggests that aerodynamic stall does not significantly influence our measurements.

Further supporting this conclusion is our analysis of the Reynolds Number (Re), calculated using the equation $Re = \rho_{N_2} v_{N_2} L_{Blade} / \mu_{N_2}$, where the dynamic viscosity of Nitrogen, μ_{N_2}, is 1.78×10^{-5} Pa·s. Here, the flow velocity of nitrogen is conservatively estimated at 52 m s^{-1} for a flow rate of 25 LPM—well above our operational range. The resulting Reynolds number of ≈ 210 indicates laminar flow conditions, as turbulent flow generally dominates at Reynolds numbers significantly higher than 2000, typically observed in pipe flows or around streamlined bodies.[41] Therefore, we assert that these common aerodynamic effects that could cause a nonlinear relationship between the rotational velocity and the flow rate are negligible in our system.

Measurement systems may potentially introduce nonlinearity into experimental results if the equipment employed exhibits inherent nonlinear characteristics. To ensure the integrity of our data, we have rigorously verified that all tools used to measure flow rate and rotor frequency are linear throughout their operational ranges, particularly at the extremes of these ranges. Consequently, we can confidently assert that any nonlinear characteristics observed in our results are not attributable to the measurement systems we used.

We propose that the observed nonlinear increase in rotational velocity as a function of flow rate can be attributed to the combined effects of nonlinear viscous damping[42] and friction at the rotor-stator interface.[43] The stabilizing medium in the gap between the rotor and stator creates a fluid coupling that reduces direct contact friction, providing smoother rotational motion and enhancing energy transfer from the flow to the rotor. This coupling helps maintain a steady speed increase by providing consistent mechanical friction.

As flow rate increases, the fluid coupling becomes more efficient in transferring energy to the rotor, resulting in a nonlinear increase in rotational velocity. The polydimethylsiloxane hydrocarbon stabilizing medium exhibits shear-thinning behavior, meaning its viscosity decreases with increasing shear rate.[42] As the flow rate increases, the rotor spins faster, causing a higher shear rate in the stabilizing medium, which reduces viscosity. This reduction in viscosity decreases the damping force and allows the rotor to spin faster. Therefore, the decreasing viscosity due to shear thinning contributes to a nonlinear increase in rotational velocity with increasing flow rate.

Additionally, the rotor-stator interface exhibits a combination of boundary and hydrodynamic lubrication regimes, as described by the Stribeck curve.[43] Initially, at lower flow rates, friction is relatively high due to boundary lubrication. However, as flow rate increases, the lubrication regime shifts toward full hydrodynamic lubrication, reducing friction nonlinearly and allowing the rotor to spin faster.

Although the mass of the stabilizing agent is non-negligible compared to the rotor and adds inertia, the fluid coupling ensures more uniform acceleration. The increase in rotational velocity follows a nonlinear trend due to the interplay between increased

Table 1. Comparison of microscale anemometers based on sensing mechanism, sensing range, input requirements, output sensor, device volume, and mounting position.

	Sensing Mechanism	Sensing Range [LPM]	Input Requirement	Output Sensor	Device Volume [mm^3]	Mounting Position	
1	Reflective Rotor	10–20	Simple: Signal light	Simple: Optical intensity	5.04×10^{-4}	Any	This Work
2	Heated Silicon Film	0.24–1.90[a]	Complex: Heating laser, signal light	Complex: Spectrum analysis	7.85×10^{-5}	Any	[24]
3	Triple FP Resonators	33.49–149.06[a]	Complex: Scanning laser	Simple: Optical intensity	5.89×10^{-3}	Any	[26]
4	Suspended fiber-plate FP resonator	9.5×10^{-6}–3.8×10^{-5}[b]	Simple: Signal light	Complex: Spectrum analysis	8.84[c]	Top-down (gravity assisted)	[25]
5	Cantilever optical fiber transducer	2–10	Simple: Signal light	Simple: Optical intensity	11.01[c]	Top-down, (gravity assisted) both sides of flow	[28]
6	Cantilever Fiber Bragg Grating with Target	0.0095–0.041[a]	Complex: Resonant wavelength (tunable laser)	Simple: Optical intensity	42.41	Top-down, (gravity assisted)	[29]
7	Cantilever Differential Fiber Bragg Gratings	83.33–360.00	Simple: Signal light	Complex: Spectrum analysis	10.1	Any	[30]

[a] Converted from m s^{-1} wind speed measurements using the geometry of our test set-up nozzle; [b] Converted from µm s^{-1} water flow using the geometry of our test set-up nozzle; [c] Some dimensions were estimated from images/renders in the manuscript.

flow rate and the nonlinear reduction of mechanical friction and viscous damping. This nonlinear friction behavior at the rotor-stator interface, combined with the shear-thinning damping effect, results in a net increase in rotational velocity with increasing flow rate, as described by the second-order polynomial equation presented in Figure 8.

Developing a physics-based model to predict the frequency response of the sensor, especially to capture the relevant nonlinear relationships observed in our experiments, is a complex task that requires further analysis. The nonlinear frequency response likely arises from intricate interactions between the sensing device, the stabilizing medium, and the operating environment, all of which introduce complexities that are not captured by the linear model based on classical dynamics. To develop an accurate theoretical model, it is necessary to consider the nonlinear damping characteristics of the stabilizing medium, microfluidic forces, and detailed aerodynamic interactions between the rotor and stator. Therefore, while our current analysis provides a foundational understanding, a more comprehensive model will be pursued in future work to fully characterize the nonlinear dynamics and further advance the application of this technology.

While linear sensor systems offer more predictable responses and simpler calibration requirements, nonlinear systems, such as the fiber tip anemometer presented here, provide several key advantages. Nonlinear systems exhibit a broader measurement range due to their nonlinear response characteristics.[44] At high flow rates, the nonlinear response curve amplifies small changes, providing high sensitivity to subtle variations. At lower flow rates, the system's nonlinear response remains sensitive by adapting dynamically to larger variations in incident flow. Thus, the second-order polynomial relationship between flow rate and sensor output allows for accurate measurement across a wider range of flow rates. Furthermore, nonlinear systems can exhibit increased sensitivity due to the nature of their response curve.[45] In the nonlinear anemometer presented in this study, the second-

order polynomial response curve shown in Figure 8 inherently provides varying levels of sensitivity at different flow rates. At specific flow rates, the response curve shows steep slopes, indicating high sensitivity to small changes in flow rate. For instance, in Figure 8, the sensitivity of the flow sensor between 16.72 and 17.55 LPM is seven times higher than the sensitivity between 12.61 and 13.43 LPM. Due to the steeper slopes in the nonlinear response curve, small changes in flow rate led to significant changes in measured rotational velocity. This characteristic enables the detection of subtle changes, even at flow rates that might not be detectable with linear sensors. The findings of this study will inspire future research into engineering nonlinear damping—the fourth dimension—in optomechanical sensors, to enhance the sensitivity of sensing elements within the user-defined range of interest.

When compared to other designs presented in the literature, this microscale anemometer offers several unique advantages. Our device features relatively simple input and output sensing hardware requirements, a small volume, and the ability to sense high flow rates. Compared to more complex mechanisms and larger devices listed in **Table 1**, our design presents a promising path for a miniaturized, mass-producible sensor within the reported flow regimes. These characteristics suggest that our anemometer could be particularly advantageous for applications requiring compact, cost-effective, and high-performance flow sensing solutions.

3. Conclusion

In conclusion, we investigated a dynamic fiber tip anemometer with a 3D rotor that revolves around a stator fabricated using a two-photon nanomachining process. The anemometer is monolithically integrated onto the cleaved face of an optical fiber that serves as an integrated waveguide. Nonlinear damping—the fourth dimension of our design—is realized by introducing a

polydimethylsiloxane hydrocarbon stabilizing agent into the gap between the rotor and stator assisted by monolithically integrated dual-function microfluidic channels. This enhancement enables consistent periodic measurement of gaseous nitrogen flow rates between 10 and 20 LPM. The dynamic nature of our sensing element allows for precise measurement of gaseous fluid flow with a minimal sensor footprint at the point of detection. Since no optical resonance is required, it supports a variety of light sources and measurement devices without requiring specific wavelengths or broad-spectrum capabilities. This high degree of adaptability significantly reduces the overall cost of an optimized, full-fledged sensor system compared to laser-based sensors, offering a compact, versatile, and cost-effective solution for advanced flow sensing applications. Comprehensive characterization of the response with and without the stabilizing medium demonstrates its critical role in regulating the dynamics between the rotor and stator, ensuring reliable and periodic sensing. Additionally, systematic analysis reveals key factors influencing the anemometer's nonlinear response. The results emphasize the advantages of nonlinear systems in sensing and provide a foundation for future research into engineering nonlinear damping to enhance sensitivity within user-defined ranges. This work paves the way for exploring highly integrated sensing elements with complex, compact, and dynamic 3D mechanical and optical components, laying the groundwork for next-generation nonlinear optomechanical sensing applications in space-limited environments.

4. Experimental Section

Computer Aided Design (CAD) Software: Each device was designed using Solidworks 3D CAD software. The solid model was divided into thin layers by the DeScribe slicer software provided by Nanoscribe GmbH.

Computational Fluid Dynamics (CFD) Analysis: The CFD analysis conducted in this study was primarily illustrative, aimed at visualizing the dynamics involved in the experiments without quantifying any specific parameters. The analysis utilized the default solid material settings.

Boundary Conditions:

– Inlet: The flow velocity was set at 20 m s^{-1}.
– Outlet: Zero gauge pressure was specified to prevent backflow.
– Interfaces/Walls: A no-slip condition was applied to mimic the interaction between the fluid and the solid boundaries.

Material Properties:

– Fluid: Nitrogen was selected as the working fluid, using standard properties from the Fluent library.

Computational Approach:

– Governing Equations: The Navier–Stokes equations, which describe the motion of fluid substances, were employed to model the flow.
– Solver: The analysis was performed using Ansys Fluent.
– Mesh Type: A triangular tetrahedral mesh was utilized.
– Mesh Refinement: The mesh was qualitatively refined, reaching the maximum number of elements allowed by the student version of Ansys.

Preparation of the 2PP Process on a Fiber Tip: A Corning SMF-28e+ optical fiber was initially prepared by cleaving it with a Fujikura CT-30 high-precision fiber cleaver. The fiber was then secured into a Newport FPH-S fiber chuck, allowing ≈0.5 mm of the fiber to extend beyond the end of the chuck. A drop of UV-curable resin, specifically Nanoscribe's IP-DIP, was

Table 2. Sputtering settings used to deposit the gold reflective coating on the flow sensor.

Parameters	Values
Cathode Power	100 Watt
Cathode Mode	DC
Burn-in Time	30 s
Burn-in Pressure	10 mTorr
Deposition Pressure	5 mTorr
Stage Rotation	5 rpm
Fiber Position	Center Stage
Deposition Time	300 s

applied to the end of the fiber chuck, fully enveloping the fiber tip. Subsequently, the chuck was attached to a custom 3D-printed jig, which was then mounted onto a 2-inch wafer plate provided by Nanoscribe. This plate was chosen for its three accessible threaded holes, facilitating secure mounting. The assembly was then adjusted so that the laser aperture, equipped with a custom 63x objective lens, made direct contact with the resin droplet on the fiber tip. The cleaved face of the fiber was manually positioned by the operator to align precisely with the laser focus. To enhance adhesion to the fiber face, a 5 µm thick pad was incorporated at the base of the optical cavity. The height of this adhesion pad was manually set by the operator to sit just below the fiber's surface, ensuring that polymerization occurred as close to the fiber surface as possible. This setup effectively secured the polymerized structure to the fiber, optimizing the integrity and stability of the fabrication.

2PP Process Description: In the 2PP process, a 780 nm femtosecond laser featuring a 120-fs pulse duration, an 80 MHz repetition rate, 40% laser power, and a scan speed of 10 mm s^{-1} was employed. The laser, directed by galvanometric control, was used to solidify the photosensitive resin. To facilitate the alignment of the device on the fiber tip, red light from a flashlight was coupled into the fiber to illuminate the fiber core. A small disk on each device served as an alignment mark, which was aligned with the core to ensure the device was accurately centered on the fiber tip. This alignment was achieved by focusing the laser inside the fiber, where the light was visible but not yet causing polymerization of the resin.

Sputtering Settings to Deposit Gold Film: A Kurt J. Lesker Company LAB 18 magnetron plasma sputtering system was utilized for the deposition of a gold film on the flow sensor. The specific parameters used for gold deposition are detailed in **Table 2**.

RPM and mTorr were used to provide the most accurate reproductions of the settings used on the fabrication equipment, where 1 rpm is equal to 0.1047 rad s^{-1} and 1 Torr is equal to 133.322 Pa.

Removal of Support Material and Masking Cube: The support material was meticulously removed by securing the fiber in a Newport FPH-S side-loading fiber chuck, which was then positioned into a Newport 561-FC fiber chuck holder. This assembly was placed beneath a Micromanipulator probe station within a stainless-steel block. Removal was facilitated using a Jmicro Technology KRN-09S magnetic probe arm paired with a Pacific Instruments ST-1 semiconductor analysis probe with a 100 nm diameter tip. The masking cube was removed using the same procedure, exposing the core of the fiber as displayed in Figures 3e and 4a.

Stabilizing Agent: The terms "stabilizing medium," "stabilizing agent," "damping medium," and "damping agent" were used interchangeably throughout this article. The chosen stabilizing agent was silicone oil, which was formulated with 85–95% low volatile petroleum (LVP) aliphatic hydrocarbon and 1–5% polydimethylsiloxane. Aliphatic hydrocarbons were compounds consisting mainly of carbon and hydrogen atoms, arranged in straight chains, branched chains, or non-aromatic rings. They were known for being less reactive compared to aromatic hydrocarbons. LVP aliphatic hydrocarbons have low volatility, meaning they have a higher boiling point and evaporate slower than other hydrocarbons. This property makes them useful in applications where minimal evaporation was

2400080 (12 of 15)

**ADVANCED
SCIENCE NEWS**

www.advancedsciencenews.com

**ADVANCED
SENSOR
RESEARCH**
Open Access

www.advsensorres.com

Table 3. The peak frequency responses from both experimental runs of the sensor.

Reference Flow Meter	Run 1 Frequency Response	Run 2 Frequency Response	Average Response	Standard Deviation
[LPM]	[Hz]	[Hz]	[Hz]	[Hz]
12.61	2.4	2.425	2.4125	0.0125
13.43	2.925	4.4	3.6625	0.7375
14.24	6.55	5.825	6.1875	0.3625
15.07	12.325	7.5	9.9125	2.4125
15.89	17.1	10.625	13.8625	3.2375
16.72	23.15	15.375	19.2625	3.8875
17.55	32.275	23.025	27.65	4.625

desired, such as in lubricants. Polydimethylsiloxane belongs to a group of polymeric organosilicon compounds that were commonly referred to as silicones. The structure of polydimethylsiloxane was typically represented as [-Si(CH₃)₂-O-]_n, showing a silicon-oxygen backbone with pendant methyl groups. It was known for its flexibility, low toxicity, thermal stability, and hydrophobic characteristics. It provides excellent lubrication, was stable over a wide range of temperatures, and was resistant to water and many chemicals. When these two components were combined, the LVP Aliphatic Hydrocarbon acts as a carrier or diluent, enhancing the material's ability to spread and reducing the overall viscosity of the mixture. Meanwhile, the polydimethylsiloxane provides the main mechanical stabilizing properties, adds thermal stability, and contributes to the chemical inertness of the oil. This combination makes this material suitable for a variety of applications, including mechanical stabilization in environments where both lubrication and stability were critical under varying temperature and pressure conditions. In the context of optomechanical fiber anemometry, this polydimethylsiloxane hydrocarbon helps stabilize the mechanical parts while ensuring that the oil's properties remain consistent during operation. The polydimethylsiloxane hydrocarbon stabilizing medium in this work was commercially available under the trade name 3-IN-ONE Silicone Oil.

Measurement Setup: The optomechanical fiber tip anemometer was characterized using the experimental setup described in Figure 6. A 6015-3 optical circulator from Thorlabs, Inc. was utilized to isolate the reflection spectrum from the flow sensor. This optical circulator, a standard fiber-optic device, transmitted light from ports 1 to 2 and from 2 to 3, experiencing ≈1 dB of insertion loss. It also prevented transmission in the opposite direction, achieving ≈40 dB of attenuation. A fiber-coupled superluminescent diode (SLD) broadband source, the Thorlabs S5FC1550SP-A2, was connected to port 1. This source emitted a spectrum of 200 nm centered at 1550 nm. The reflection spectrum from the flow sensor was subsequently isolated and routed through port 3 of the optical circulator to an optical power meter and a digital oscilloscope. The reference flow meter utilized in this study was the 4112K49 model with aluminum fittings from McMaster-Carr. This flow meter has a measurement range of up to 23.7 LPM for gaseous nitrogen and features an accuracy of ±3% of the indicated value.

Uncertainty Analysis: To further support the interpretation of our results, an analysis of the measurement was included uncertainty. While the standard deviation was reported in Figure 8b as an estimate of the expected measurement range, the importance of providing additional context for the potential variability in our data was recognized. Therefore, a table was provided below that lists the minimum, maximum, and average measurements, offering a broader perspective on the variability observed in our experimental data.(Table 3)

LPM was used in this work to facilitate comparisons with the reference flow meter, where one LPM is equal to 6×10^4 m³ s⁻¹.

Statistical Analysis: *Pre-processing*: The raw data from the photodetector was subjected to several pre-processing steps during analysis. First, the absolute value of the data was taken to remove measurements near the noise floor of the instrument that appeared negative and could interfere with further processing. Next, the minimum and maximum intensity values from each measurement were used to normalize the intensity values, scaling them between one (at the minimum) and one hundred (at the maximum) using $M_{new} = \frac{M-min}{max-min} \times (100 - 1) + 1$.

To ensure clarity in the data pre-processing steps, the variables used in the normalization formula were defined as follows:

- M: The raw intensity measurement from the photodetector at a given point in time.
- min: The minimum intensity value recorded during a single measurement cycle.
- max: The maximum intensity value recorded during the same measurement cycle.
- M_{new}: The normalized intensity value, scaled between 1 and 100, representing the processed measurement after normalization.

Explanation:

- $M - min$: This represents the difference between the raw intensity value and the minimum recorded intensity for the measurement cycle, effectively shifting the data to start at 0.
- $max - min$: This was the range of the intensity values within the measurement cycle, used to scale the difference between M and min.

This pre-processing method helps to standardize the data for subsequent analysis, ensuring that all measurements were on a consistent scale and ready for further processing, such as frequency analysis using a Fast Fourier Transform (FFT).

Next, the logarithm of the data was applied. This step was taken to enhance the frequency analysis by amplifying reflection events logarithmically, ensuring that reflection events of varying intensity, but clearly above zero, were given equal weight in the frequency-domain analysis. This approach significantly improved the accuracy of the frequency domain analysis. The different intensities of these non-zero reflection events on a linear scale are illustrated in Figure 7d–i. Subsequently, the logarithmically scaled data was subjected to an FFT using the SciPy library in Spyder 5.4.1 from the Anaconda Python distribution. The intensity output of the FFT was then normalized between zero and one, resulting in the data displayed in Figure 8a.

The average of the four frequencies with the highest intensity from the normalized FFT was calculated and reported as the dominant frequency response for each measurement. This approach helps to account for some of the spectral blur observed at higher flow rates, which it attributed to the shaking of the fiber in our experimental test setup.

Data Presentation: In Figure 8b, the squares represent the mean value of the dominant frequency response from two experimental measurements at each flow rate. The error bars indicate ±1 standard deviation from the mean of these two measurements. The orange line represents a polynomial fit to the mean values, calculated using the NumPy library in Spyder 5.4.1 from the Anaconda Python distribution. The coefficient of determination (R^2) was reported as a measure of the fit quality, indicating that a high proportion of the variation can be explained by the calculated polynomial.

Sample Size: Two experimental runs were conducted for the same device across the same flow rates, resulting in a sample size of two for the data presented in Figure 8b.

On a fundamental level, it was highly confident that increasing the flow rate leads to an increase in the device's frequency response. This confidence was supported by the results from a One-Way Analysis of Variance (ANOVA), which indicates that the variation between flow rates was 10.91 times greater than the variation within flow rates, as represented by the F statistic of 10.91. The F statistic measures the ratio of variance between the groups (different flow rates) to the variance within the groups, with a

Table 4. The results of one-way ANOVA evaluating the effect of flow rate on the measured frequency responses.

SUMMARY

Groups	Count	Sum	Average	Variance
12.61	2	4.825	2.4125	0.000312
13.43	2	7.325	3.6625	1.087812
14.24	2	12.375	6.1875	0.262813
15.07	2	19.825	9.9125	11.64031
15.89	2	27.725	13.8625	20.96281
16.72	2	38.525	19.2625	30.22531
17.55	2	55.3	27.65	42.78125

ANOVA

Source of Variation	SS	df	MS	F	P-value	F crit
Between Groups	1001.109	6	166.8516	10.91954	0.002959	3.865969
Within Groups	106.9606	7	15.28009			
Total	1108.07	13				

higher value indicating a greater degree of difference between the groups. The resulting P-value of 0.003 quantifies the probability that the observed relationship between flow rate and response frequency was due to chance, with a low P-value indicating a statistically significant relationship. The Data Analysis Add-in for Microsoft Excel was used to perform this calculation, and the results are presented in **Table 4** below, which includes both the summary statistics and the ANOVA results.:

Explanation of Summary and ANOVA Table Contents: The Summary table provides essential descriptive statistics for each group analyzed. The "Groups" column lists the different categories of the independent variable, in this case, the distinct flow rates. The "Count" indicates the number of observations within each group, reflecting the sample size for each flow rate. "Sum" represents the total sum of all measured values within each group, while "Average" provides the mean value of these observations, offering insight into the central tendency of each group. The "Variance" column measures the variability within each group, indicating how much the observed values deviate from their group mean.

The ANOVA table presents the results of the Analysis of Variance, which assesses whether there were statistically significant differences between the group means. The "Source of Variation" differentiates between "Between Groups"—which accounts for the variation due to differences between group means—and "Within Groups"—which accounts for variation within each group, often attributed to random error or other factors. "SS" (Sum of Squares) quantifies the total variation, while "df" (Degrees of Freedom) denotes the number of independent values that contribute to the analysis. "MS" (Mean Square) represents the average variation, calculated by dividing the sum of squares by the corresponding degrees of freedom.

The "F" statistic, derived from the ratio of the mean square between groups to the mean square within groups, indicates the extent to which the group means differ relative to the variability within the groups. A higher F value suggests a greater likelihood that the differences between group means were significant. The "P-value" quantifies the probability that the observed differences occurred by chance, with a lower P-value (typically less than 0.05) indicating statistical significance. Finally, the 'F crit" (Critical Value of F) represents the threshold value that the F statistic must exceed to reject the null hypothesis, confirming the presence of significant differences between the groups.

These tables collectively provide a comprehensive analysis of the relationship between flow rate and frequency response, supporting the conclusion that the device's frequency response was significantly influenced by changes in flow rate. The results presented in the manuscript do successfully showcase the fundamental operation of the device with high sta-

tistical confidence and demonstrate the successful implementation of the stabilizing agent.

Software Used: The NumPy and SciPy libraries were used in Spyder 5.4.1 from the Anaconda Python distribution and Microsoft Excel with the Data Analysis Add-in to perform this analysis.

Conflict of Interest

The authors declare no conflict of interest.

Data Availability Statement

The data that support the findings of this study are available from the corresponding author upon reasonable request.

[1] G. Li, G. Li, S. Yang, L. Ji, Q. Sun, J. Su, C. Wu, *Sens. Actuators A, Phys.* **2022**, *347*, 113970.

[2] S. Tang, M. Zou, C. Zhao, Y. Jiang, R. Chen, Z. Xu, C. Yang, X. Wang, B. Dong, Y. Wang, C. Liao, G. Xu, *Biosensors* **2022**, *12*, 391.

[3] J. W. Smith, J. C. Williams, J. S. Suelzer, N. G. Usechak, H. Chandrahalim, *J. Micromech. Microeng.* **2020**, *30*, 125007.

[4] H. Chandrahalim, J. Smith, Temperature-Immune Self-Referencing Fabry-Pérot Cavity Sensors, US10,942,313B2, **2021**.

[5] J. Williams, J. Smith, J. S. Suelzer, N. G. Usechak, H. Chandrahalim, in 2020 IEEE Sensors, IEEE, Rotterdam, Netherlands **2020**, pp. 1–4.

[6] H. Huang, X. Zhu, C. Jiang, H. Chen, J. Song, Y. Wang, S. Sun, *Appl. Opt.* **2023**, *62*, 275.

[7] J. W. Smith, J. S. Suelzer, N. G. Usechak, V. P. Tondiglia, H. Chandrahalim, in *2019 20th Int. Conf. Solid-State Sensors, Actuators Microsystems & Eurosensors XXXIII (Transducers & Eurosensors XXXIII)*, IEEE, Berlin, Germany **2019**, pp. 64–9652.

[8] J. C. Williams, H. Chandrahalim, J. S. Suelzer, N. G. Usechak, *Adv. Photonics Res.* **2022**, *3*, 2100359.

[9] J. C. Williams, H. Chandrahalim, in *Optical Sensors and Sensing Congress*, Optica Publishing Group, Vancouver, British Columbia **2022**, SM1C.4.

[10] S. Pevec, D. Donlagic, *Opt. Express* **2022**, *30*, 41999.

[11] T. Y. Cosgun, A. Dzipalski, C. A. Ross, R. R. Thomson, M. Kingston, S. Brooks, W. N. MacPherson, *Opt. Express* **2022**, *30*, 42923.

**ADVANCED
SCIENCE NEWS**

www.advancedsciencenews.com

**ADVANCED
SENSOR
RESEARCH**
Open Access

www.advsensorres.com

[12] A. L. Hendriks, D. Rabelink, M. Dolci, P. Dreverman, M. S. Cano-Velázquez, L. Picelli, R. P. J. van Veldhoven, P. Zijlstra, E. Verhagen, A. Fiore, *Optica* **2024**, *11*, 512.

[13] Y. Zhang, X. Ma, B. Xu, J. Li, H. Chen, J. Kang, C. Zhao, S. Jin, *Opt. Lett.* **2024**, *49*, 2197.

[14] H. Huang, C. Liao, M. Zou, D. Liu, S. Liu, Y. Wang, Z. Bai, D. Liu, B. Li, J. Huang, F. Wang, J. Zhou, C. Zhao, X. Weng, L. Liu, J. Qu, Y. Wang, *ACS Photonics* **2023**, *10*, 1916.

[15] Y. Tong, C. Pan, Z. Li, H. Chen, D. Xue, L. Cheng, Y. Zhen, T. Zhang, Y. Gao, L. Zhang, X. Guo, L. Tong, P. Wang, *Opt. Express* **2024**, *32*, 14674.

[16] C. Han, H. Ding, B. Li, L. Shi, H. Xu, *Rev. Sci. Instrum.* **2022**, *93*, 045001.

[17] X. Guo, Q. Yao, X. Zhang, P. Wang, L. Sun, Y. Li, F. Yu, X. Zhao, *IEEE Sens. J.* **2024**, *24*, 12374.

[18] C. Saavedra, D. Pandey, W. Alt, D. Meschede, H. Pfeifer, *Phys. Rev. Appl.* **2022**, *18*, 044039.

[19] J. C. Williams, H. Chandrahalim, J. S. Suelzer, N. G. Usechak, *ACS Appl. Mater. Interfaces* **2022**, *14*, 19988.

[20] J. Williams, H. Chandrahalim, Optical Fiber Tip Micro Anemometer, US11,635,315B2, **2023**.

[21] J. Williams, J. S. Suelzer, N. G. Usechak, H. Chandrahalim, in *2020 IEEE Sensors*, IEEE, Rotterdam, Netherlands **2020**.

[22] J.-H. He, C.-H. He, M.-Y. Qian, A. A. Alsolami, *Sens. Actuators A, Phys.* **2024**, *376*, 115664.

[23] H. H. Bruun, *Meas. Sci. Technol.* **1996**, *7*, 024.

[24] G. Liu, W. Hou, W. Qiao, M. Han, *Opt. Express* **2015**, *23*, 13562.

[25] Y. Guan, X. Dong, *IEEE Sens. J.* **2022**, *22*, 23915.

[26] Y. Liu, Z. Jing, Q. Liu, A. Li, W. Li, S. Zhang, A. Lee, F. Tian, R. Li, W. Peng, *iScience* **2022**, *25*, 104402.

[27] C. Zhao, D. Liu, Z. Cai, B. Du, M. Zou, S. Tang, B. Li, C. Xiong, P. Ji, L. Zhang, Y. Gong, G. Xu, C. Liao, Y. Wang, *Biosensors* **2022**, *12*, 168.

[28] E. Schena, P. Saccomandi, S. Silvestri, *Rev. Sci. Instrum.* **2013**, *84*, 024301.

[29] M. Ding, T. Zhang, R. Wang, D. Su, X. Qiao, *IEEE Sens. J.* **2023**, *23*, 3609.

[30] Y. Zhao, Y.-F. Gu, R.-Q. Lv, Y. Yang, *IEEE Trans. Instrum. Meas.* **2017**, *66*, 502.

[31] Y. O. EL-DIB, N. S. ELGAZERY, *Fractals* **2020**, *28*, 2050095.

[32] M. Yao, Y. Zhang, X. Ouyang, A. P. Zhang, H.-Y. Tam, P. K. A. Wai, *Opt. Lett.* **2020**, *45*, 3516.

[33] S. Lightman, O. Porat, G. Hurvitz, R. Gvishi, *Opt. Lett.* **2022**, *47*, 5248.

[34] H. Chandrahalim, J. C. Williams, J. W. Smith, J. S. Suelzer, N. G. Usechak, in *2019 IEEE Res. Appl. Photonics Def. Conf. RAPID*, IEEE, Miramar Beach, FL, USA **2021**, p. 1.

[35] J. Williams, H. Chandrahalim, Hinged Temperature-Immune Self-Referencing Fabry-Pérot Cavity Sensors, US11,320,596B2, **2022**.

[36] J. Williams, H. Chandrahalim, Method of Making Hinged Self-Referencing Fabry-Pérot Cavity Sensors, US11,287,575B2, **2022**.

[37] J. Williams, H. Chandrahalim, Hengky, Monolithically Integrated Microscale Pressure Sensor on an Optical Fiber Tip, US11,326,970B2, **2022**.

[38] J. D. Anderson Jr., *Fundamentals of Aerodynamics*, McGraw-Hill, New York City, New York, USA **2010**.

[39] H. B. Musgrove, M. A. Catterton, R. R. Pompano, *Anal. Chim. Acta* **2022**, *1209*, 339842.

[40] D. Bratton, D. Yang, J. Dai, C. K. Ober, *Polym. Adv. Technol.* **2006**, *17*, 94.

[41] F. M. White, *Fluid Mechanics*, McGraw-Hill, New York City, New York, USA **2015**.

[42] M. Venczel, G. Bognár, Á. Veress, *Processes* **2021**, *9*, 331.

[43] M. Woydt, R. Wäsche, *Wear* **2010**, *268*, 1542.

[44] N. Kacem, J. Arcamone, F. Perez-Murano, S. Hentz, *J. Micromech. Microeng.* **2010**, *20*, 045023.

[45] J. Zhao, C. Sun, N. Kacem, H. Wang, R. Gao, P. Liu, Y. Huang, *J. Appl. Phys.* **2018**, *124*, 164503.